

Thermal and Visual Tracking of Photovoltaic Plants for Autonomous UAV inspection

Luca Morando, Carmine Tommaso Recchiuto, Jacopo Calla, Paolo Scuteri and Antonio Sgorbissa

Abstract—Since the demand for renewable solar energy is continuously growing, the need for more frequent, precise, and quick autonomous aerial inspections using Unmanned Aerial Vehicles (UAV) may become fundamental to reduce costs. However, UAV-based inspection of Photovoltaic (PV) arrays is still an open problem. Companies in the field complain that GPS-based navigation is not adequate to accurately cover PV arrays to acquire images to be analyzed to determine the PV panels' status. Indeed, when instructing UAVs to move along a sequence of waypoints at a low altitude, two sources of errors may deteriorate performances: (i) the difference between the actual UAV position and the one estimated with the GPS, and (ii) the difference between the UAV position returned by the GPS and the position of waypoints extracted from georeferenced images acquired through Google Earth or similar tools. These errors make it impossible to reliably track rows of PV modules without human intervention reliably. The article proposes an approach for inspecting PV arrays with autonomous UAVs equipped with an RGB and a thermal camera, the latter being typically used to detect heat failures on the panels' surface: we introduce a portfolio of techniques to process data from both cameras for autonomous navigation. Experimental tests performed in simulation and an actual PV plant are reported, confirming the validity of the approach.

Index Terms—Autonomous Navigation, Unmanned Aerial Vehicle (UAV), Photovoltaic (PV) plant inspection

I. INTRODUCTION

WE are currently facing a worldwide energy challenge that requires us to search for alternatives to fossil fuels, including green and renewable energies [1]. According to [2], in 2019, renewable energy sources made up 34% of gross electricity consumption in the EU-27, slightly up from 32% in 2018. While wind and hydropower accounted for two-thirds of the total electricity generated from renewable sources (35% each), the remaining one-third of the electricity generated was from solar power (13%), solid biofuels (8%), and other renewable sources (9%). The analysis also shows how solar power is the renewable source experiencing the fastest growth, given that in 2008 it accounted for around 1%.

Solar energy presents many advantages since it is environmentally friendly, has a long life, requires low maintenance, is noise-free and clean. However, photovoltaic (PV) installations need a periodic maintenance since they always need to be in optimal conditions to work properly [3]. Surface defects [4], [5], [6], [7], [8] are the most common ones and can be detected through human inspection: a qualified operator can easily detect different defects including snail trails, yellowing

of the encapsulant, delamination and bubble formation in the encapsulant, front surface soiling, junction box connection corrosion, busbar oxidation, or impact from physical objects. However, human inspection might be time-consuming if the PV array is very large (or in particular conditions, e.g. panels are mounted on a rooftop). To reduce the cost and time required for maintenance, methods exist [9] to estimate the presence and impact of global defects through the analysis of the power output. However, this kind of approach presents two main disadvantages: a reference power production is required, and the exact locations of defects cannot be identified.

Researchers have recently proposed the use of Unmanned Aerial Vehicles (UAV) for PV inspections. In the past decades, research made big steps forward concerning the development of UAVs for monitoring applications, including the inspection of power transmission lines [10], gas and oil pipelines [11], precision agriculture [12], and bridges [13]. The ability of multirotor UAVs to hover and move freely in the air, the fact that they can be easily piloted and equipped with different sensors make this technology very appealing in monitoring scenarios. Generally, UAVs used for PV inspection are equipped with a thermal camera to identify different types of defects that can produce heat anomalies on the solar panels (which may or may not complement a standard RGB camera or other sensors).

The use of UAVs reduces the inspection time but, on the other hand, creates a larger amount of raw data to be processed, which must meet given requirements in terms of resolution and position accuracy. To ensure that requirements are met, UAVs are still manually piloted for PV inspections, even when considering large solar plants: however, the possibility of autonomously controlling UAVs over those sites in a reliable way might dramatically improve their performances and reduce the need for human resources. The use of GPS can help achieve more autonomy: ideally, it would be sufficient to provide a sequence of waypoint coordinates to the UAV mission planner before take-off. The waypoints might, on their turn, be chosen during the pre-flight setup, with an operator drawing the desired path on Google Earth images showing the solar farm to be inspected. However, as discussed in [9], the error in planimetric coordinates between objects captured in Google Earth and obtained from a map produced by ground surveying techniques ranges from 5 to 10 meters. This aspect, related to the intrinsic inaccuracy of the received GPS signal by the UAV, will likely conduct to an erroneous estimation of its position, determine an erroneous alignment of the UAV with the PV module rows, increase the amount of useless data acquired, and reduce performances.

Based on these premises, it is straightforward that a more

L. Morando, C. Recchiuto, A. Sgorbissa are with University of Genova; J. Calla and P. Scuteri are with JPDroni S.r.l. Contact author: antonio.sgorbissa@unige.it

advanced methodology, which uses the UAV sensors information to correct in real-time the error between the UAV and the actual position of PV modules, is needed.

The main contribution of this article is a portfolio of techniques for PV module segmentation and UAV navigation through visual servoing based on the onboard RGB and thermal cameras. Please notice that, in PV plant inspection, a thermal camera is required for detecting defects: then, developing a system using both RGB and thermal cameras to collect data looks particularly convenient as it may improve reliability in critical light or temperature conditions [9]. JP Droni¹, which contributed to this work as part of its own RTD activities, confirms that GPS-based navigation is the only approach currently adopted in Italy (and, to the best of their knowledge, in the world) for PV inspection. However, visual servoing techniques based on PV module segmentation are mandatory when the UAV flies at a lower altitude to acquire higher-resolution images: in this case, positioning errors might severely affect the possibility for the UAV to keep the PV modules to inspect within the camera frame.

The system at work is shown in Figure 1, showing the main concepts that will be used in the rest of the article.

- *PV midline*, a straight line in the middle of the PV module row that determines the desired motion direction.
- *PV end*, a point on the PV midline that identifies the end of the PV module row.
- *PV start*, a point that identifies the start of the new PV module row, whose position is computed with respect to the end of the previous row.

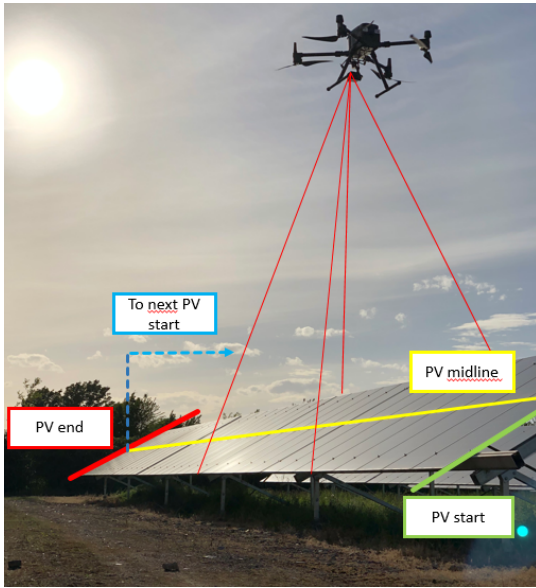


Fig. 1. System at work in a real PV plant. The DJI Matrice 300 drone was equipped with a hybrid RGB and thermal camera, the DJI Zenmuse XT2.

Section II surveys the relevant literature. Section III describes the general system architecture. Section IV introduces the techniques used for PV module segmentation using RGB

and thermal images. Section IV-C briefly discusses a procedure for the optimization of segmentation thresholds. Section V introduces strategies for UAV autonomous navigation. Section 7 presents experimental results in a photorealistic simulated environment and a real PV plant. Finally, in Section 8, conclusions and directives for future research are drawn.

II. STATE OF THE ART

Despite limitations in terms of positioning accuracy, GPS-based path-planning still play a crucial role in this context. In [14] an approach to generate an optimal waypoint path based on satellite images is proposed to reduce the error due to the misalignment of georeferenced images and the actual inspection site. The PV plant's boundary is extracted via computer vision techniques, and the system can re-compute the path if the UAV requires reaching a specific location (e.g., a PV module where a defect is detected during the inspection). In [15] a novel technique for boundary extraction is proposed using a VGG16 backbone fully convolutional neural network. The network is trained on the AMIR dataset [16], a collection of aerial imagery of PV plants from different countries. These and similar approaches focus on planning the initial waypoint path to cover the PV plant but underestimate the problem of guiding the UAV to move autonomously along such path for the automatic detection of solar cell faults.

Various techniques and applications have been proposed for automatic defect detection from aerial images. For example, the authors of [17] and [18] use computer vision and machine learning techniques to detect and classify cracks and potholes in roads and highways from UAV images. The work described in [19] is capable of detecting defects in aerial power lines via Faster RCNN [20] using UAV-acquired images. Similarly, [21] describes the real-time inspection of power lines through UAVs using a Hough Transform [22] for cable detection. Strategies for automatic defect detection have also been applied to the PV plant scenario. For example, [23] proposes two different techniques for inspection and mapping: aerial IR/visual image triangulation and terrestrial IR/visual image georeferencing. The authors discuss the potential of both approaches in detecting defective PV modules. In [24], a deep learning-based solution for defect recognition is used, exploiting the use of aerial images obtained from UAVs. Convolutional neural networks are used to classify various forms of visible defects. A similar approach is presented in [25] where two region-based CNNs are unified to generate a robust detection approach that combines thermography and telemetry data for panel condition monitoring. In [26] a model-based approach is proposed for the detection of panels, which relies on the structural regularity of the PV arrays and introduces a novel technique for local hot spot detection from thermal images, based on the use of a fast and effective algorithm for finding local maxima in the PV panel regions. In [27] a fully automated approach for the detection, classification, and geopositioning of thermal defects in the PV modules is proposed, using a novel method based on image reprojection and function minimization to detect the panels from the images. These and similar works address only the problem of autonomous defect detection, without

¹JP Droni Srl is a company in Genova providing aerial services for video productions, precision agriculture, and technical inspection of power plants.

using the acquired images as a feedback for the UAV to move autonomously along the inspection path. The UAV is either manually controlled or moves along a set of predefined waypoints using GPS data only [28] with a consequent impact on data quality [29].

Visual Servoing is a technique widely used in robotics, and many examples of UAV autonomous navigation based on data acquired through cameras exist in literature, some of them involving inspection tasks. For example, an algorithm for the detection of vertical features from images has been used in [30] to guide a UAV along a semi-linear path while flying over a highway in the US. This approach is based on the consideration that vertical edges are a characterizing attribute of highways that can be easily detected using methods such as RANSAC [31], which can also be used to predict splines [32] where sharp curves may occur. Similar techniques may be found in [33] and [34], where the authors respectively give their contribution in the field of precision agriculture and building inspection. In [33], a novel control technique based on the development of a passivity-based visual servoing controller with dynamics compensation for the tracking of crops is described. The proposed system allows the autonomous navigation of a UAV along straight lines such as the one formed by structured crops. In [34], a complete navigation and inspection task is executed by a completely autonomous quadrotor. The most interesting part of this work is the approach used for road detection and navigation, which consists in segmenting the image in predominant color layers before feeding it to DeepLabv3+ [35], a network trained for semantic segmentation. road is then identified in the image and finally followed by the UAV by defining a sequence of control points. These techniques have not been applied to UAV navigation over large PV plants. This may also be due to the complexity of the scenario, which may have different characteristics in terms of the number of PV module rows, their dimension and mutual arrangement.

A few examples of UAV autonomous navigation over PV plants have been presented in recent years. For example, in [36], the authors propose a method based on the edge detection of PV modules. The approach extracts vertical edges from RGB images using a Hough Transform: then, the detected misalignment between the PV midline observed from images and the actual UAV position is fed to the navigation control law. Unfortunately, this approach have only been tested in simulation. An edge detection technique is also used in [37], where the metallic profile of the PV array is detected and segmented by combining color and feature extraction, using the Hough Transform and a Hue-Saturation-Value (HSV) model: once the *PV midline* has been computed, the UAV's velocity orthogonal to the PV module row is controlled to keep it aligned with it. Both approaches rely on parameters for edge extraction, which shall be manually tuned and reconfigured at each inspection: notwithstanding these limitations, it is worth noticing that, in the "era of Deep Learning", many of the abovementioned approaches [33], [34], [37], [34], [36] rely on model-based vision techniques for feature segmentation. In structured environments whose model is a priori known, such in the case of PV plants, a model-based formulation

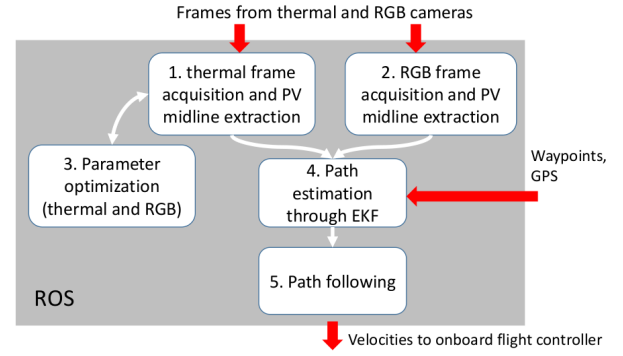


Fig. 2. System architecture implemented in ROS.

of the problem may offer advantages in terms of predictable and explainable behaviour [38], and possibly robustness to adversarial attacks [39], that cannot be ignored. As an aside, this is also confirmed by the fact that AI (and in particular Machine Learning) in aviation is still at the beginning: even if AI is quite widespread in subdomains like logistics and fuel consumption estimation [40], [41], AI-techniques in flight control can be hardly found in real-world application scenarios.

III. SYSTEM ARCHITECTURE

The proposed system is capable of autonomous, UAV-based PV inspection based on the following core elements.

- A procedure for detection of PV modules in real-time using a thermal or an RGB camera (or both).
- A procedure to correct errors in the relative position of the *PV midline*, initially estimated through GPS, by merging thermal and RGB data acquired in real-time.
- A navigation system provided with a sequence of georeferenced waypoints defining an inspection path over the PV plant, which uses the estimated position of the *PV midline* to make the UAV move along the path with bounded navigation errors.

The software architecture implemented in ROS [42] is represented in Figure 2, where the relationships between different ROS nodes are shown. Nodes (1) and (2) acquire and process raw frames from the RGB and the thermal camera and perform PV module segmentation. To this end, they execute some intermediate steps discussed in Sections IV-A and IV-B. As an output to this process, each node returns the parameters of a straight line running in the middle of a PV module row. To increase segmentation accuracy and reduce dependence on environmental factors, node (3) implements an optimization procedure to find the best parameters for segmentation: some details about this procedure are in Sections IV-C. Node (4) merges subsequent observations, independently performed by the two cameras in subsequent time instants. Since each observation may be affected by errors, an Extended Kalman Filter (EKF) is used to estimate the *PV midline* by merging a priori knowledge in the form of georeferenced waypoints and run-time observations provided by nodes (1) and (2), see Sections V-A and V-B. Finally, node (5) uses the estimated reference path for controlling the UAV along its path through visual servoing, see Section V-C.

PV module row tracking is not sufficient: we need rules to instruct the UAV to move to the next row when the previous one has been completely inspected. That is, we need a waypoint-based reference path defining the order according to which PV module rows shall be inspected. Remind that waypoints may be labelled as *PV start* or *PV end*, both acquired before operations through Google Earth or other georeferenced images (and possibly affected by positioning errors), Figure 1. Then, waypoints shall be connected in a sequence such that

- the path goes from a *PV start* to a *PV end* waypoint when moving along the same PV row: in this case, the distance between *PV start* and *PV end* define how far a *PV midline* extracted in real-time shall be followed before moving to the next one;
- the path goes from a *PV end* to a *PV start* waypoint when jumping to the next PV row: in this case the relative position of *PV start* with respect to *PV end* defines the start of the new row with respect to the previous one.

Currently, waypoints are manually chosen but this process might be automated starting from a georeferenced image of the whole plant ([14], [15]).

As already discussed, real-time segmentation and visual tracking of PV module rows may play a key role in succesful navigation, since waypoint-based navigation using only the embedded positioning system of the UAV (typically merging GPS, IMUs, and compass) has well-known limitations: the absolute position of *PV start* and *PV end* waypoints, as well as GPS data, may be affected by large errors with respect to the world frame. On the opposite, by using visual servoing to move along a PV row, we only need to ensure that the relative position of adjacent waypoints and the small UAV displacement from a PV row to the next one performed with GPS only are sufficiently accurate. This assumption looks reasonable because georeferenced waypoints computed from Google Earth images and GPS data may be affected by large biases (which, in the the case of GPS, vary with time) but tend to be locally coherent – i.e., the relative error of waypoints (respectively, GPS-data) respect to previous waypoints (respectively, GPS-data acquired in nearby locations) is small.

Finally, even if it is not the focus of this article, remark that additional high-resolution thermal images (not used for navigation) are captured and stored in the onboard storage of the UAV for future processing aimed to defect detection. In this case, the frequency of acquisition is determined by the UAV flying height to guarantee that images are overlapping for subsequent stitching.

IV. DETECTION OF PV MODULES

A. Segmentation of PV modules via thermal camera

Each image captured by the thermal camera can be represented as a matrix with given width and height. The reference frame F lies in the upper left corner of the image plane and $f(u, v)$ is a function that associates a thermal value to each pixel (u, v) : thermal cameras return the thermographic image as a mono-channel grayscale intensity matrix, where the pixels intensities may assume values between 0 and 255.

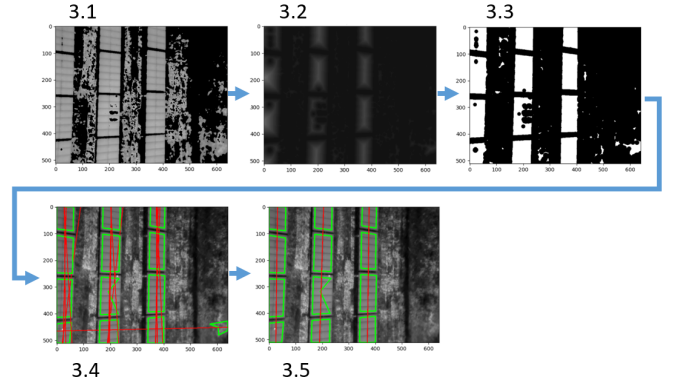


Fig. 3. Pipeline for PV module detection from thermal images: 1) thresholded image; 2) distance matrix; 3) binarized image; 4) segmentation and regression line extraction; 5) clustering and *PV midline* estimation.

As a first step, we analyze typical thermal values of pixels characterizing PV panels, and choose two thresholds th_1 and th_2 (with $0 < th_1 < th_2 < 255$) that define this intensity range. Then, each image pixel can be processed as follows:

$$f(u, v) = \begin{cases} f(u, v), & \text{if } th_1 < f(u, v) < th_2 \\ 0, & \text{otherwise.} \end{cases} \quad (1)$$

Thresholds are chosen starting from empirical results obtained through the analysis of previously acquired images, in our case a dataset acquired with a DJI Zenmuse H20T during manual PV plant inspections and composed of 430 thermal images with 640×512 dimensions. Before starting operations, it is possible to tune these threshold more accurately through the optimization procedure described in Section IV-C, in order to define a range that better models the plant to be inspected in the current environmental conditions. As expected and visible in Figure 3.1, the application of this mask is not sufficient to make the the PV modules emerge unambiguously. In fact, in some regions, the ground has the same temperature as the panels, making the detection of the PV modules difficult.

As a second step, we filter noise out by exploiting a priori domain knowledge: even if pixels with thermal intensity in the selected range can be found also outside PV panels, still a panel is expected to be characterized by a higher density of pixels falling within the thresholds. Then, the entire image is filtered by computing a distance (dissimilarity) matrix D that stores the Euclidean distance of each pixel in F from the nearest zero value. That is, for each pixel (u, v) , we compute:

$$d(u, v) = \sqrt{(u_{zero} - u_d)^2 + (v_{zero} - v_d)^2} \quad (2)$$

where u_{zero} and v_{zero} are, respectively, the row and the column of the zero value pixel nearest to (u, v) , Figure 3.2.

As a third step, each pixel of the distance matrix D is transformed into a binary intensity value as follows:

$$b(u, v) = \begin{cases} 255, & \text{if } d(u, v) > th_3 \\ 0, & \text{otherwise} \end{cases} \quad (3)$$

where th_3 can be interpreted as a distance threshold to determine whether a pixel (u, v) in the original image F belongs or not to a high density region, Figure 3.3. The threshold th_3 is

set a priori and then fine-tuned with the optimization procedure described in Section IV-C. Groups of neighbouring pixels are then clustered into N polygonal regions S_i : during the process, only the regions that are larger than a given number of pixels survive, whereas smaller clusters are deleted².

As a fourth step we compute, for each segmented region S_i , a regression line through polynomial curve fitting³: starting from regions S_i , N regression lines are computed, each described by a point $p_i = (u_i, v_i)$ and a unitary vector l_i defining a direction in the image plane F , Figure 3.4.

In the fifth step, the core of the detection algorithm requires clustering all the extracted regression lines that are likely to correspond to PV modules aligned in the same row. That is, starting from a subset of individual shapes S_i and the corresponding regression lines, a unique cluster C_j (more robust to noise) is computed with $j = 1, \dots, J$. Specifically, two regions S_i and S_k are clustered in C_j if the corresponding regression lines meet the two conditions below:

- The magnitude of the difference vector $\|l_i - l_k\| < th_4$, i.e., the two lines tend to be parallel.
- The average point-line distance between all pixels in the image plane belonging to the first line and the second line $dist(p_i, l_i, p_k, l_k) < th_5$, i.e., the two lines tend to be close to each other.

Parameters th_4 and th_5 depend on a priori geometrical consideration and not on environmental conditions, and therefore their are not subject to optimization before operations. Clustering is iteratively repeated for all shapes S_i : then, a new regression line is computed for each cluster C_j , Figure 3.5. The final output of the process is a set of J lines, each possibly corresponding to multiple PV modules belonging to the same row. In the image frame, each observed *PV midline* is represented through a couple of points $o_j = (p'_j, p''_j)$, with $p'_j = (u'_j, v'_j)$, $p''_j = (u''_j, v''_j)$ corresponding to the intersection of the line with the borders of the image.

B. Segmentation of PV modules via RGB camera

The algorithm developed to process thermal images is almost completely reused for RGB images, with the only exception of the initial steps required for PV module segmentations, Figures 4.1 and 4.2.

When using RGB images, the rows of PV modules are detectable for their blue color in contrast with the background – the same could not be said if they were built over a lake or the sea. Then, as a first step, the original image F is mapped onto the HSV color space: Figure 4 shows the results, RGB-rendered by using H values for the R channel, S for G, and V for B. As a second step, the PV modules are segmented from the background by thresholding values in each of the three HSV channels, Figure 4.2. As previously, the lower HSV thresholds th_4, th_5, th_6 and the higher HSV thresholds th_7, th_8, th_9 are manually chosen based on a priori domain knowledge and then fine-tuned before operations as explained in Section IV-C. The resulting image is converted to a mono-channel binary image.

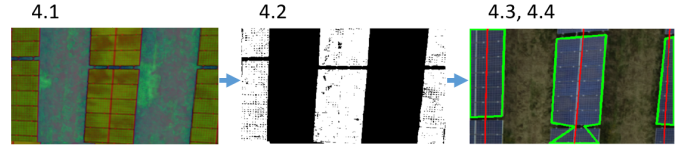


Fig. 4. Pipeline for PV module detection from RGB images: 1) Mapping onto HSV space; 2) binarized image; 3,4) segmentation, regression line extraction and clustering, PV midlines estimation.

The final steps of the process, as for thermal images, require to segment polynomial regions S_i, \dots, S_N , each associated with a regression line, that are finally clustered into J clusters C_j each corresponding to an observed line $o_j = (p'_j, p''_j)$, Figures 4.3 and 4.4.

C. Thresholds tuning

PV module detection needs appropriate thresholding. For thermal images, we need to choose the lower and upper bounds th_1 and th_2 of thermal intensity in (1) and the distance threshold th_3 in (3); for RGB images, we need to choose the minimum th_4, th_5, th_6 and maximum th_7, th_8, th_9 values for each HSV channel. For this purpose, we implemented an optimization algorithm that maximizes the number of PV modules detected in thermal and RGB images separately taken, as well as the matching between the PV modules detected in both images. In the following, it is assumed that thermal and RGB images are overlapping, which can be obtained by computing a roto-translation and a scaling between the two frames, if needed. Under this constraint, despite the segmented PV module shapes may be slightly different depending on the acquisition method used⁴, they are expected to roughly occupy the same regions in pairwise images.

The algorithm used to minimize the cost function is L-BFGS-B [43], a limited-memory algorithm that can be used to minimize a non-linear cost function subject to simple bounds on the variables (the algorithm is particularly appropriate to solve large non-linear, non-convex optimization problems in which the Hessian is hard to compute).

We assume that the UAV reaches the start position of the first PV module, possibly remotely controlled by a human operator, with its front oriented towards the direction of the PV modules row. Then, the following non-linear, non-convex optimization problem on variables th_i , $i = 1 \dots 9$, is solved:

$$\min_{th_1 - th_9} - \sum_{i=1}^{N_1} (c_{i,1} + r_{i,12}) - \sum_{i=1}^{N_2} (c_{i,2} + r_{i,21}) \quad (4)$$

subject to

$$0 \leq th_i \leq max_i \quad (5)$$

where (4) is the cost function, whose value expresses the “quality” of the segmentation algorithm given a set of thresholds $th_1 - th_9$, and max_i is the upper bound on the corresponding variable.

⁴In thermal images, the temperature of the junctions between adjacent PV panels may be different from PV panels themselves, resulting in a sequence of smaller rectangular shapes. In RGB images, this never happens, returning larger rectangular areas composed of multiple panels.

²We use the OpenCv function `findContours`.

³We use the OpenCv function `fitLine`.

Mathematical details of the cost are not discussed for sake of brevity. Intuitively, please remember that the thermal camera (sensor number 1) computes a set of N_1 segmented regions S_i , $i = 1 \dots N_1$, and the RGB camera (sensor number 2) computes a set of N_2 segmented regions S_i , $i = 1 \dots N_2$. Then the first sum in the cost function refers to regions extracted from the thermal camera and the second sum refers to regions extracted from the RGB camera. For each region S_i extracted from thermal images, the cost function comprises two terms $c_{i,1}$ and $r_{i,12}$. The former term intuitively takes into account how close S_i is to a rectangular shape oriented along the current direction of motion, and how close is S_i 's extension to a value that depends on the PV module geometry and the UAV height from the ground. The latter term measures the pixel-wise correlation between the region S_i and the binary mask extracted from the paired RGB image covering the same area (i.e., it is higher if the region S_i segmented from the thermal image is also present in the RGB image). The two terms $c_{i,2}$ and $r_{i,21}$ are computed in an analogous way, starting from regions extracted from RGB images.

Please notice that jointly optimizing all variables might be time-consuming: for this reason, during experiments in PV plants, we decompose the problem (4) into two sub-problems. Firstly, we consider RGB images only and search for the minimum of $-\sum_{i=1}^{N_2} c_{i,2}$: that is, we ignore correlation with thermal images. Secondly, we consider thermal images only and search for the minimum of $-\sum_{i=1}^{N_1} (c_{i,1} + r_{i,12})$. This simplification looks a good compromise to reduce computation time, which may be relevant if we want to repeat the procedure, e.g., at the *PV start* of each new row,

V. UAV NAVIGATION

A. From the image frame F to the camera frame C

To describe the motion of the UAV body with respect to the world frame, we define a mobile camera frame C with origin in the center of the camera lens, xy -plane parallel to the uv -image plane at distance f (focal length), x -axis pointing to the UAV front, and z -axis downward⁵. The origin of the camera frame moves as the drone moves along the PV module row: since the UAV is endowed with a gimbal mechanism that keeps the xy -plane of the camera frame parallel to the XY -plane of the world frame, all the transformations involving the image, world, or camera frame are simpler since the camera is always looking perpendicularly to the ground in a nadiral position.

Given a point $p_i = (u_i, v_i)$ in the image frame, its position (x_i^C, y_i^C) in the camera frame C can be computed as:

$$x_i^C = -\frac{k}{f}(v_i - \frac{V}{2})z_g^C \quad (6)$$

$$y_i^C = \frac{k}{f}(u_i - \frac{U}{2})z_g^C \quad (7)$$

where k converts the pixel size in meters and z_g^C is the distance of the ground from the origin of the camera frame.

Using the formula above, for every observed line $p_j' = (u_j', v_j')$, $p_j'' = (u_j'', v_j'')$ in the image frame F returned by

the procedure in Section IV, we compute the parameters $o^C = (a^C, b^C)$ of an observed line $y^C = a^C x^C + b^C$ in the camera frame C through simple geometrical considerations. Please notice that we can ignore the z^C coordinate because the xy plane of the camera frame is parallel to the ground thanks to gimbal stabilization: the UAV altitude will be separately controlled through an independent mechanism. Then, the implicit equation $y^C = a^C x^C + b^C$ should be better interpreted as the equation of a plane perpendicular to the xy plane of the camera frame, to which the UAV must converge.

B. Path estimation through EKF

The observations $o^C = (a^C, b^C)$, performed using the thermal and RGB cameras as the UAV moves along the PV module row, are iteratively merged to estimate the *PV midline* parameters in the world frame, described as a straight line with implicit equation $y^W = a^W x^W + b^W$ (once again, this should be better interpreted as a plane perpendicular to the ground).

For this purpose, an Extended Kalman Filter [44] is used. The state $m^W = (a^W, b^W)$ of the *PV midline* is described in the world frame W in order to keep the system dynamics constant: in this case, the state m^W to be estimated does not change as the UAV moves along the PV module row since the latter is obviously not moving. However, the observations $o^C = (a^C, b^C)$ acquired through cameras are expressed in the camera frame and therefore the system needs to know the UAV pose in order to map them on the world frame through the EKF observation matrix H . In this work, we assume that the position x^W, y^W and yaw θ^W of the camera frame with respect to the world frame are computed by the low-level flight controller embedded in the UAV, which typically merges GPS, IMUs, and compass (once again, thanks to the gimbal mechanism and the fact that we control the altitude through an independent mechanism, z^w is ignored since the pitch and roll of the camera are zero). Using the embedded UAV positioning system may be counterintuitive, since we repeatedly stated it is affected by absolute errors. However, in this phase, it is deemed appropriate since here we are not interested in knowing the absolute UAV pose with great accuracy: it is sufficient that the pose error slowly changes in time and is almost constant during the whole inspection (which typically happens with GPS low-frequency errors), to guarantee that subsequent observations are coherent with each other and do not produce abrupt changes in the state estimate⁶.

The EKF allows for merging observations acquired at different times originated from the thermal and RGB camera. In the following, we use the notation $\hat{m}_{k+1|k}^W = \hat{m}_k^W$ to describe the evolution of the state at the prediction step $k+1$ due to control inputs (which, as already mentioned, is constant), and the notation $o_{k+1}^C = (a_j^C, b_j^C)$ to describe the observation made at the update step $k+1$ by the j^{th} sensor, where $j = 1, 2$ correspond, respectively, to the thermal and RGB cameras.

During the update step, we need a measurement model $\hat{o}_{k+1}^W = H_{k+1} \hat{m}_{k+1|k}^W$, where H_{k+1} is the Jacobian of the

⁶Ideally, we could attempt to estimate the UAV pose in the world frame by merging the sensors above with the observations made with cameras, by hypothesizing an augmented state vector including both the PV midline and the UAV pose [45]. However, this possibility is not exploited in this work.

⁵That is, x heads towards $-v$ in the image plane and y heads towards u .

non-linear observability function $h(m)$, which allows for obtaining the expected measurement \hat{o}_{k+1}^C from the estimated state $\hat{m}_{k+1|k}^W$ given the current camera position and yaw x^W, y^W, θ^W . Specifically, $h(m^W)$ has two components:

$$\begin{aligned} h_1(m^W) &= \frac{a^W - \tan \theta^W}{1 + a^W \tan \theta^W} \\ h_2(m^W) &= \frac{x^W a^W + b^W - y^W}{\cos \theta + \sin \theta a^W} \end{aligned} \quad (8)$$

whose Jacobian with respect to (a^W, b^W) needs to be evaluated in $\hat{a}^W, \hat{b}^W, x^W, y^W, \theta^W$.

The EKF is a recursive algorithm consisting in two steps referred to as state prediction and update. The prediction at step $k+1$ can be expressed as:

$$\hat{m}_{k+1|k}^W = A\hat{m}_{k|k}^W + Bu_{k|k}, \quad (9)$$

where A , in our case, is the identical matrix and $B = 0$ since the state m^W is invariant over time when expressed in world coordinates. The state equations are linear and the EKF is needed only because of the non-linearity of the observation model. The error covariance matrix is

$$P_{k+1|k} = AP_{k|k}A^T + Q, \quad (10)$$

where the process noise $Q = 0$ since the state is not evolving.

During the update step, only those observations o_{k+1}^W that are ‘‘sufficiently close’’ to the estimated state (in the same spirit adopted for clustering in Section IV) are considered, whereas outliers are rejected to avoid undesired corrections that may be due to the detection of neighbouring PV rows running in parallel to the tracked one. The covariance of the measurement uncertainty matrix R_j relative to each sensor $j = 1, 2$ is evaluated experimentally, and takes into account both segmentation errors due to the procedure in Section IV as well as the fact that, during an inspection, the GPS error may be subject to minor variations therefore partially conflicting with the assumption of a constant GPS error in (8). In the correction step, the Kalman gain is computed starting from R and P as usual:

$$K_{k+1} = P_{k+1|k}H_{k+1}^T(H_{k+1}P_{k+1|k}H_{k+1}^T + R_j)^{-1}, \quad (11)$$

and the a posteriori estimate is updated as:

$$\hat{m}_{k+1|k+1}^W = \hat{m}_{k+1|k}^W + K_{k+1}(o_{k+1} - H_{k+1}\hat{m}_{k+1|k}^W), \quad (12)$$

$$P_{k+1|k+1} = (I - K_{k+1}H_{k+1})P_{k+1|k}. \quad (13)$$

The EKF is initialized with $\hat{m}_{0|0}^W = (a^W, b^W)$ estimated at step $k = 0$ by considering the two waypoints at the start (*PV start*) and the end (*PV end*) of the initial PV module row. Even if the state may be affected by a significant error, it will be iteratively reduced by the EKF through subsequent observations as the UAV moves.

C. Path following

Path following works differently in two different phases: (i) when the UAV is moving from *PV start* to *PV end* along a PV module row; (ii) when it is moving from *PV end* of the current row to *PV start* of the next one.

In phase (i), navigation is based on *PV midline* tracking. After each iteration of the EKF, the estimated parameters describing the *PV midline* in the world frame $\hat{m}_{k+1|k+1}^W = (\hat{a}^W, \hat{b}^W)$ are mapped back onto the camera frame for path following, yielding (a_{ref}^C, b_{ref}^C) . Then, given the equation $y^C = a_{ref}^C x^C + b_{ref}^C$ in the camera frame, the distance error

$$e = -b_{ref}^C / (a_{ref}^C + 1)^{1/2} \quad (14)$$

is computed, as well as the parallel and the perpendicular vectors to the path

$$V_{\parallel}^C = (1/a_{ref}^C, 1) \quad (15)$$

$$V_{\perp}^C = (-1, 1/a_{ref}^C). \quad (16)$$

Given the quantities above, different approaches can be used to control the distance from the *PV midline*. In this work, we adopt a simple ‘‘carrot chasing’’ approach [46], [47]: a weighted sum of the parallel and perpendicular vectors is computed to compute the position of a virtual moving target (using the distance error e as a weighting factor for V_{\perp}^C), and a PID controller is used to tune the UAV velocities to regulate the distance from the target to zero.

In phase (ii), the UAV uses the pose information x^W, y^W, θ^W returned by the onboard flight controller to move from *PV end* to the next *PV start*, based on the assumption that the relative position of adjacent waypoints as well as the small UAV displacements from a PV row to the next one are sufficiently accurate even when performed with GPS only—once again, because GPS errors are likely to be almost constant during the inspection.

In both phases, the altitude is separately controlled using embedded sensors returning the height from the ground⁷.

VI. EXPERIMENTAL RESULTS

In this section, the experiments conducted in a real PV plant and a realistic simulation environment are presented.

A. Material and Methods

Real-world experiments in a PV plant have been conducted using a DJI Matrice 300 aircraft equipped with a DJI Zenmuse XT2 camera. The camera has a field of view of 57.12×42.44 degrees and a gimbal mechanism. An onboard DJI Manifold equipped with a NVIDIA Jetson TX2 and 128GB of internal memory performs all the computations described in previous Sections to process the acquired images and control the UAV.

The simulation environment deserves more attention. In addition to the onboard DJI Manifold performing the core computations and the actual DJI Matrice (required also in simulation, as explained below), tests are performed using an external Dell XPS notebook with an Intel I7 processor and 16 Gb of RAM, required to simulate thermal and RGB image acquisition. Indeed, two programs run in parallel to simulate, respectively, the dynamics and the perception of the UAV:

⁷A method to automatically control the UAV altitude depending on the difference between the actual and expected dimensions of PV modules on the image plane has been implemented, but not discussed in this work.

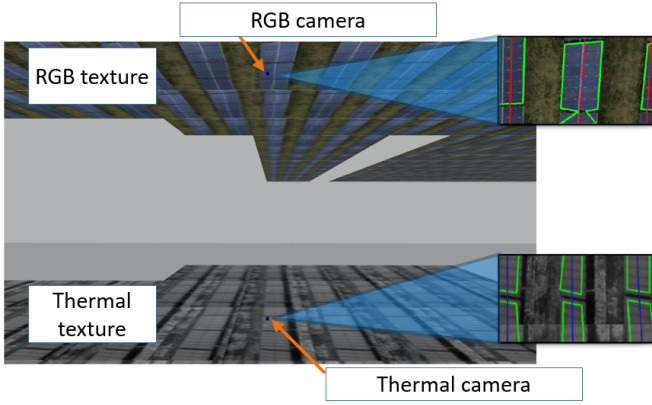


Fig. 5. Gazebo Simulator linked to the Matrice 300 DJI Simulator. Only perception is simulated, by updating the position of the RGB (looking upward) and thermal (looking downward) cameras coherently with the UAV/camera pose returned by the DJI Matrice Simulator.

- DJI Matrice Simulator, embedded in the DJI Matrice 300 and accessible by an external computer. When the DJI Manifold is connected to the drone and the OSDK is enabled, this program simulates the UAV dynamics based on the commands received from the control architecture running on the DJI Manifold.
- Gazebo Simulator, running on the external Dell XPS notebook, integrated with ROS. Here, only the camera and the related gimbal mechanism are simulated, to provide the DJI Manifold with images acquired in the simulated PV plant. The camera position inside Gazebo is linked to the camera/UAV position returned by the DJI Matrice Simulator, to guarantee coherence in the simulated images returned during the simulated flight.

In Gazebo, the simulation environment is modeled in order to create a realistic operative scenario. To simulate both cameras, textures simulating RGB images are placed “above in the sky”, while textures simulating thermal images are “below on the ground”. By adding in Gazebo two cameras, one looking at the ground and the other looking at the sky, the simultaneous acquisition of RGB and thermal images is simulated. Textures are produced from real thermal images captured by the DJI Zenmuse XT2 during a realistic PV plant inspection in northern Italy, Figure 5.

Both in real world experiments and in simulation, we initially compute the “reference waypoint path” to be followed by the UAV, by considering PV module rows one after the other in boustrophedon mode. Once the start of the first PV row has been reached, the optimization process for tuning thresholds depending on environmental conditions is executed, by letting the UAV hover at a certain height over the PV module. Then the UAV starts moving along the PV module row, using both cameras and the EKF for iteratively correcting the reference path. When the UAV reaches *PV end*, visual tracking stops, and the UAV moves to the next *PV start* using GPS only. The mission is completed when the UAV has inspected a given number of parallel PV module row.

The thermal and RGB images are processed, approximately, at a frequency of 3 and 5 frames per second, both in simulation

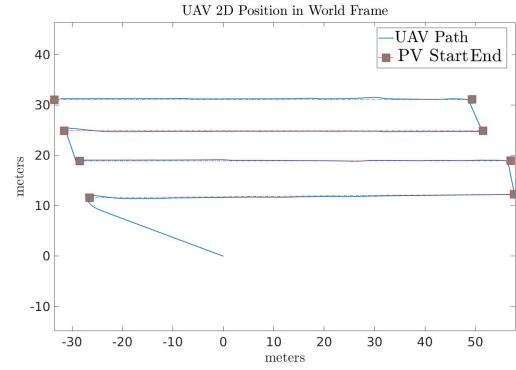


Fig. 6. Projection on the XY-plane of the UAV path (thermal camera).

and in real experiments (computations can be made more efficient to achieve a higher frame rate).

In the next Sections, results obtained during the simulated and real-world experiments conducted near Alessandria in northern Italy, are described. Simulation experiments (Section VI-B) are mainly aimed to validate the proposed approach and assess the reliability of the system in presence of inaccurate waypoint positioning. Experiments in the real scenario (Section VI-C) are mainly aimed to compare the robustness of the proposed approach with different sensor configuration and evaluate advantages deriving from a combined use of thermal and RGB cameras.

B. Experimental Results in Simulation

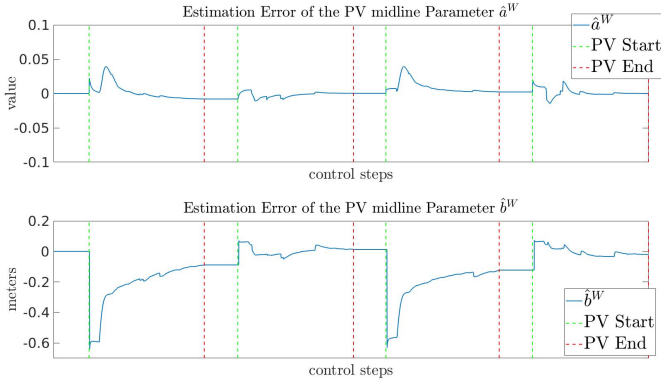
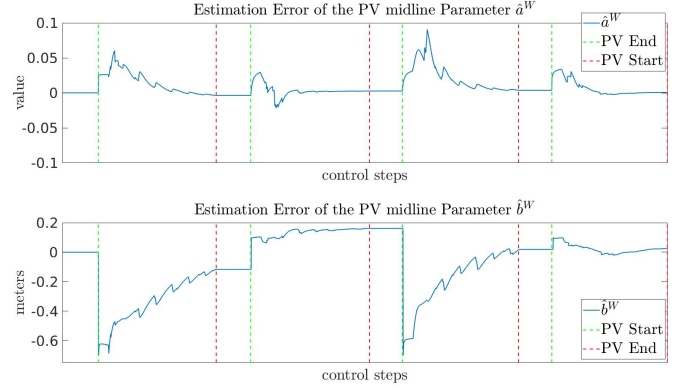
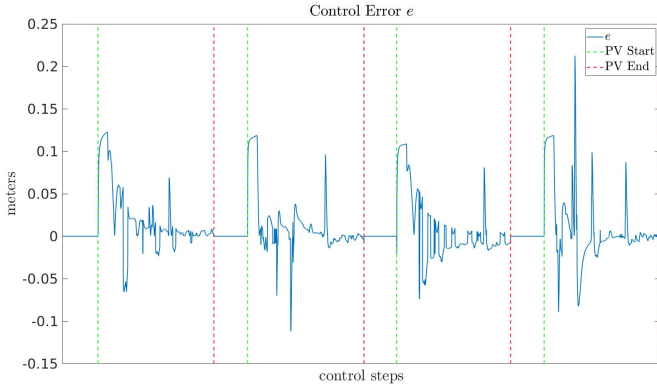
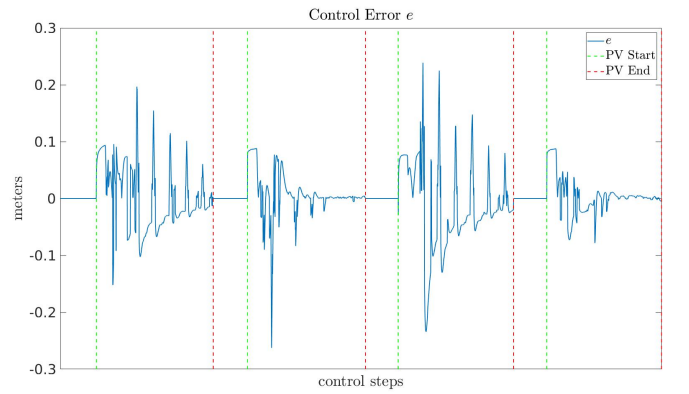
Three different classes of experiments have been performed in simulation:

- Subsection VI-B1 reports about simulated experiments with thermal camera only, RGB camera only, and both cameras for panel detection. Here we do not consider errors in waypoint positioning, which are correctly located on the midlines of the corresponding PV rows.
- Subsection VI-B2 reports about simulated experiments with both cameras to assess the robustness of the approach in presence of errors in waypoint positioning.

1) *Testing the impact of different cameras for panel detection:* Navigation is performed along four parallel PV rows. The waypoints are assumed to be correctly placed at the start and the end of each row without errors. During navigation, the UAV velocity has a constant value of $0.8m/s$, and the UAV flies at a constant height of $15m$ respect to the take-off point.

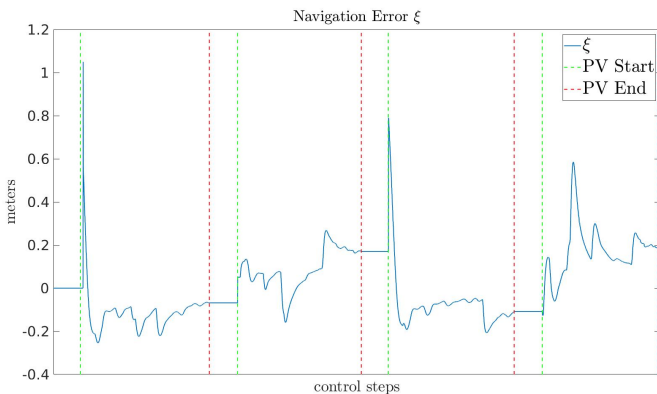
In Figure 6, the projection on the XY-plane of the UAV path along four parallel PV rows is shown. After take-off, the UAV autonomously reaches the first *PV start*, and hovers there for some second before starting navigation to collect observations to estimate the *PV midline*. Navigation performance can be evaluated by measuring the convergence of the UAV position (blue line) to the midline of PV module rows (red line).

Experiments are initially performed with the thermal camera only. In Figure 7 the error between the real PV midline $m = (a^W, b^W)$ (the ground truth is known in simulation) and the estimated state $\hat{m} = (\hat{a}^W, \hat{b}^W)$ returned by the EKF is shown. Green vertical lines correspond to *PV start*; red

Fig. 7. State of the *PV midline* estimated by the EKF (thermal camera).Fig. 10. State of the *PV midline* estimated by the EKF (RGB camera).Fig. 8. Control error from the estimated *PV midline* (thermal camera).Fig. 11. Control error from the estimated *PV midline* (RGB camera).

vertical lines correspond to *PV end* of the same row. Since the UAV moves from the end of one row to the start of the next one by using positioning information provided by the onboard flight controller, the plots included between a red vertical line and the subsequent green line shall be ignored since they correspond to a change of *PV row*.

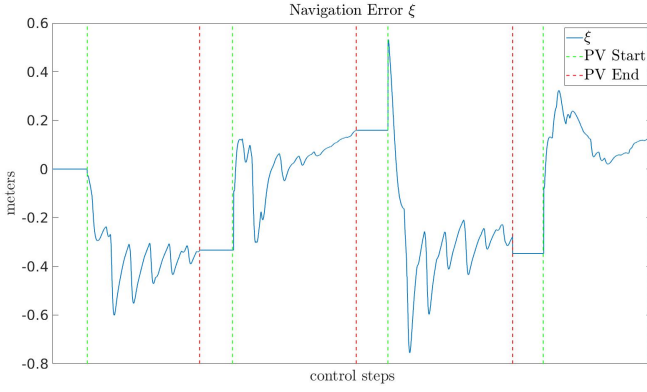
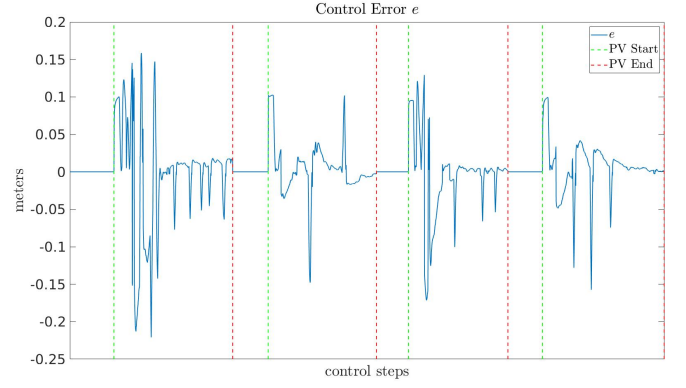
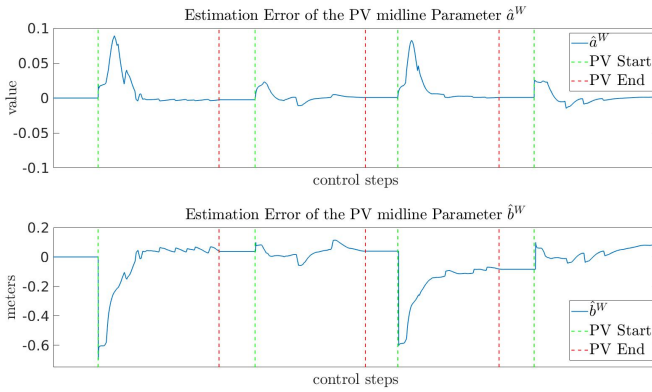
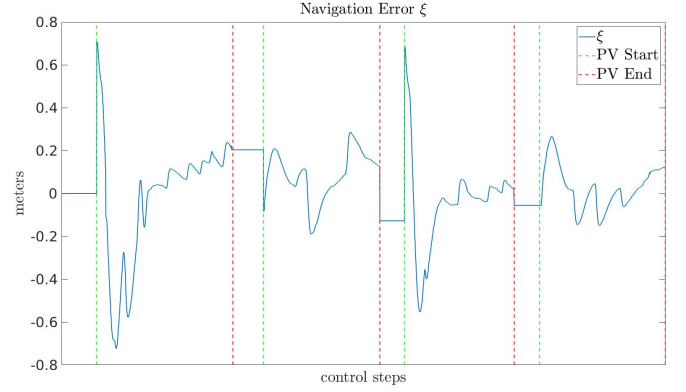
In Figure 8, the control error e between the UAV position and the *PV midline* estimated with the EKF is shown, with average $\mu_e = 0.022$ and standard deviation $\sigma_e = 0.031$ (we consider only values included between a green vertical line and the subsequent red vertical line).

Fig. 9. Navigation error from the real *PV midline* (thermal camera).

In Figure 9, the navigation error ξ between the UAV position and the actual *PV midline* (the ground truth is known in simulation) is shown. The navigation error has an average $\mu_\xi = 0.145$ and a standard deviation $\sigma_\xi = 0.132$ meters. The Figure shows that the navigation error tends to be larger when the UAV starts to track the *PV module row* after reaching *PV start*, green vertical line. This is coherent with the fact that *PV start* is considered to be reached when the UAV position is within a 1 meter distance, thus producing an initial error that is recovered later.

Next, experiments are performed with the RGB camera only. The projection on the *XY*-plane of the UAV path using the RGB camera is not reported since it is difficult to appreciate differences with the previous experiment. Figure 17 reports the error between the actual and the estimated state of the *PV midline*. Figure 11 reports the control error, with average $\mu_e = 0.032$ and standard deviation $\sigma_e = 0.036$ (i.e., performance are worst than the thermal camera in this case). Figure 12 reports the navigation error, with average $\mu_\xi = 0.201$ and standard deviation $\sigma_e = 0.157$.

Finally, experiments are performed with both cameras. Figure 13 reports the error between the actual and the estimated state of the *PV midline*. Figure 14 reports the control error, with average $\mu_e = 0.026$ and standard deviation $\sigma_e = 0.036$. Figure 15 reports the navigation error, with average $\mu_\xi = 0.137$ and standard deviation $\sigma_e = 0.150$. As expected, the presence of both thermal and RGB cameras improves

Fig. 12. Navigation error from the real *PV midline* (RGB camera).Fig. 14. Control error from the estimated *PV midline* (both cameras).Fig. 13. State of the *PV midline* estimated by the EKF (both cameras).Fig. 15. Navigation error from the real *PV midline* (both cameras).

performance with respect to using one camera only.

2) *Navigation with errors in waypoint positions:* Tests have been performed by considering large errors in the positions of waypoint at the start and the end of PV rows, to simulate inaccurate waypoint positions computed from Google Earth images. An example is shown in Figures 16 to 19, where navigation is performed using both cameras: waypoints do not correspond to *PV start* and *PV end* of actual PV module rows, but are subject to a rototranslation error plus additional noise.

By observing the actual UAV's path, blue curve in Figure 16, it can be noticed that the UAV reaches the correct *PV start* on the second, third, and fourth PV row, thus compensating large errors due to waypoint wrong placement. The control and navigation errors are comparable with the previous experiments: the control error in Figure 18 has an average $\mu_e = 0.022$ and standard deviation $\sigma_e = 0.033$. The navigation error in Figure 19 has an average $\mu_\xi = 0.109$ and standard deviation $\sigma_e = 0.114$.

C. Results in Real World Experiments

Experiments were conducted in a PV plant in Predosa in Northern Italy, exploring different configurations:

- Subsection VI-C1 explores navigation along one PV row using the thermal camera only.
- Subsection VI-C2 explores navigation along one PV row using the RGB camera only.

- Subsections VI-C3 and VI-C4 explores navigation along one/four PV rows using both thermal and RGB cameras.

In all tests, the UAV moves at a constant height from the ground of 15m at 0.6m/s (unless otherwise specified).

1) *Navigation with Thermal Camera only:* An example of PV module detection in Predosa, obtained using the thermal camera, is shown in Figure 20 on the left.

In Figure 21, the projection on the XY-plane of the UAV path is shown. After take-off, the UAV is manually guided

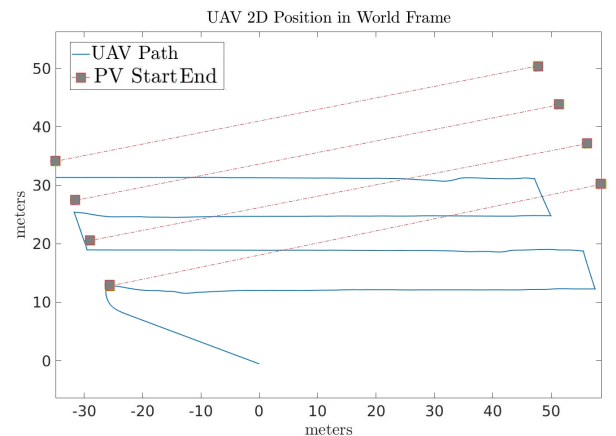


Fig. 16. Projection on the XY-plane of the UAV path in presence of waypoint positioning errors (both cameras).

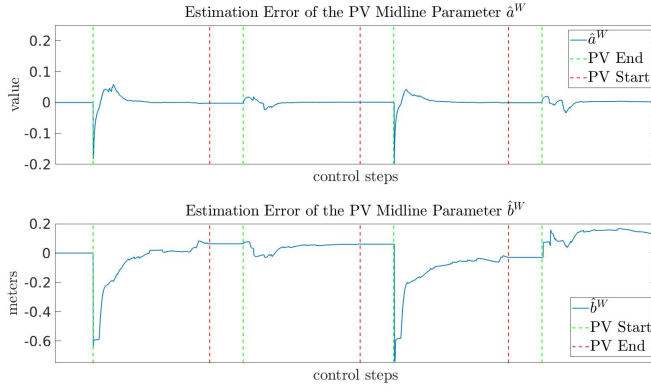


Fig. 17. State of the *PV midline* estimated by the EKF in presence of waypoint positioning errors (both cameras).

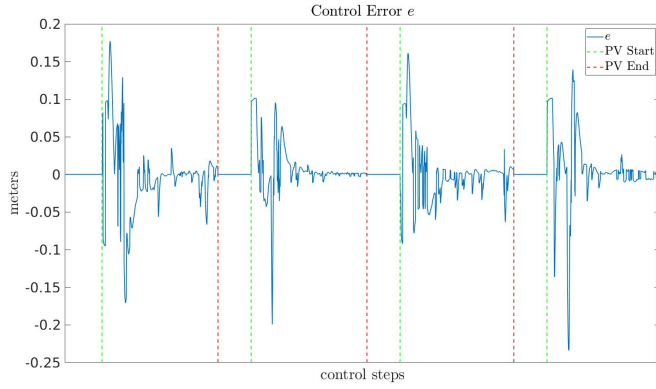


Fig. 18. Control error from the estimated *PV midline* in presence of waypoint positioning errors (both cameras).

to the first waypoint and starts collecting observations to estimate the *PV midline* through the EKF. Please notice that, in real world experiments, the position of the PV module row in the world and the corresponding *PV start* and *PV end* are estimated before operations using the onboard GPS, since the ground truth is known only in simulation. However, this information is used here only for representation purposes: during navigation, PV tracking is performed using the control method described in the previous Sections, and navigation

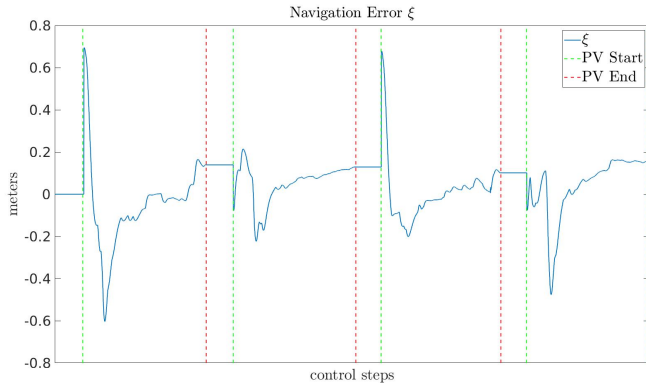


Fig. 19. Navigation error from the real *PV midline* in presence of waypoint positioning errors (both cameras).

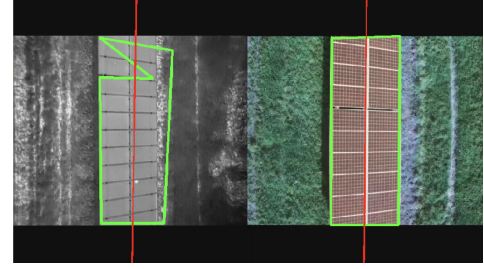


Fig. 20. PV modules detection in Predosa, Italy (15 meters from the ground).

errors are computed by manually inspecting the video stream acquired by onboard cameras as explained in the following. Despite the cloudy day making panel detection difficult, the UAV was able to navigate along the PV module row.

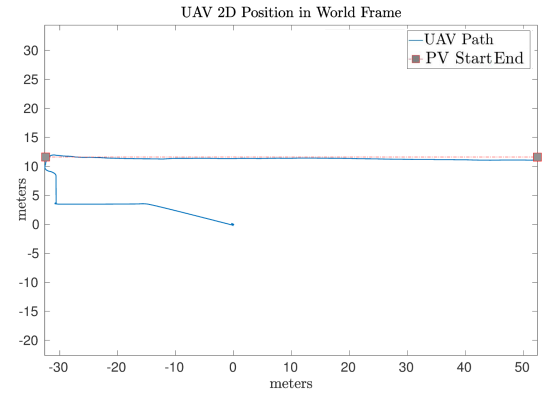


Fig. 21. Projection on the XY-plane of the UAV path (thermal camera).

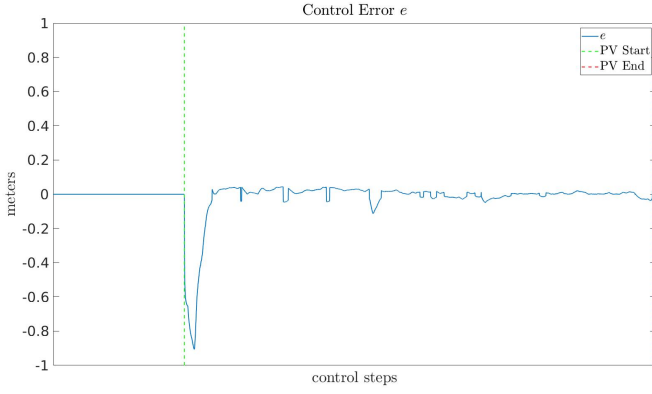
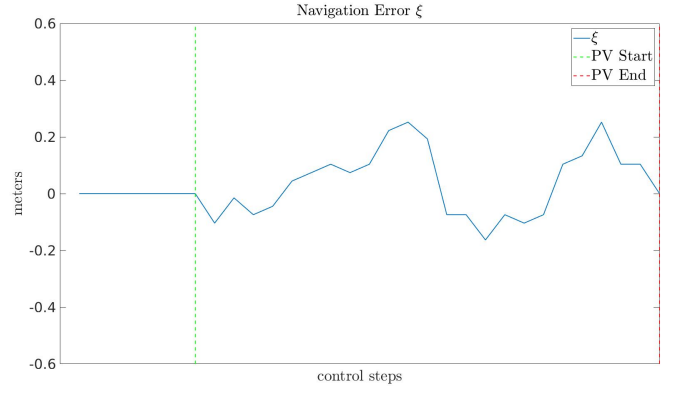
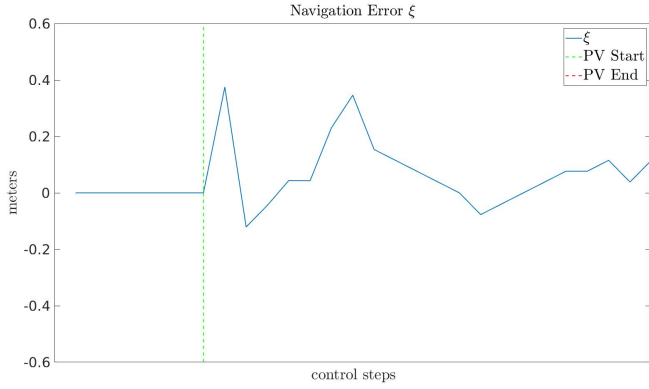
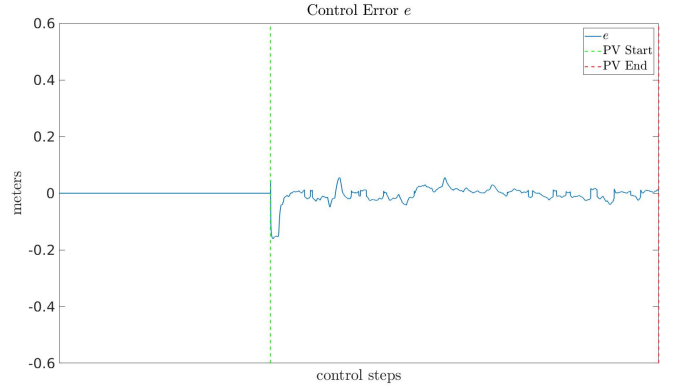
In Figure 22, the control error e is shown (i.e., the distance from the estimated *PV midline*), with a significant initial error due to inaccurate detection of the *PV midline* (which is later recovered), average $\mu_e = 0.045m$ and standard deviation $\sigma_e = 0.129m$. In Figure 23, the navigation error ξ is shown (i.e., the distance from the actual *PV midline*), with average $\mu_\xi = 0.10m$ and standard deviation $\sigma_\xi = 0.10m$. The navigation error ξ is computed differently from simulation since the ground truth is not available in this case: the video stream is sampled every 4 seconds, and images are manually inspected to measure the distance in pixels and then in meters⁸ between the center of the image and the center of the PV module row (ξ tends to zero as this distance tends to zero).

2) *Navigation with RGB Camera only:* An example of PV module detection using the RGB camera only is shown in Figure 20 on the right.

The projection on the XY-plane of the UAV path is not reported since it would be difficult to appreciate differences with the previous test. In Figure 24, the control error e is shown, with average $\mu_e = 0.034m$ and standard deviation $\sigma_e = 0.060m$. In Figure 25, the navigation error ξ is shown, with average $\mu_\xi = 0.11$ and standard deviation $\sigma_\xi = 0.16$.

3) *Navigation with both cameras:* The same test has been performed again with both thermal and RGB cameras used for

⁸The meters/pixel ratio is computed by knowing the width in meters of a PV module and measuring its corresponding width in pixels in the image.

Fig. 22. Control error from the estimated *PV midline* (thermal camera).Fig. 25. Navigation error from the real *PV midline* (RGB camera).Fig. 23. Navigation error from the real *PV midline* (thermal camera).Fig. 26. Control error from the estimated *PV midline* (both cameras)

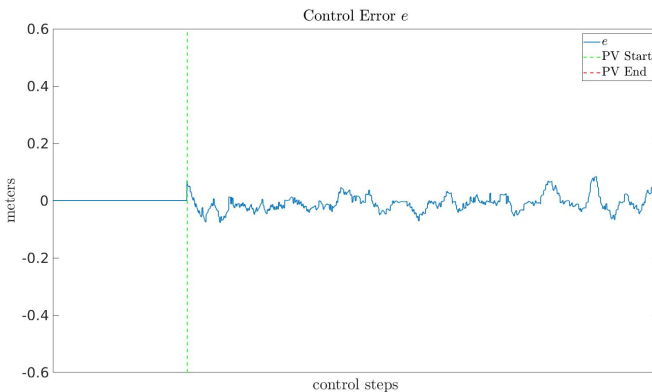
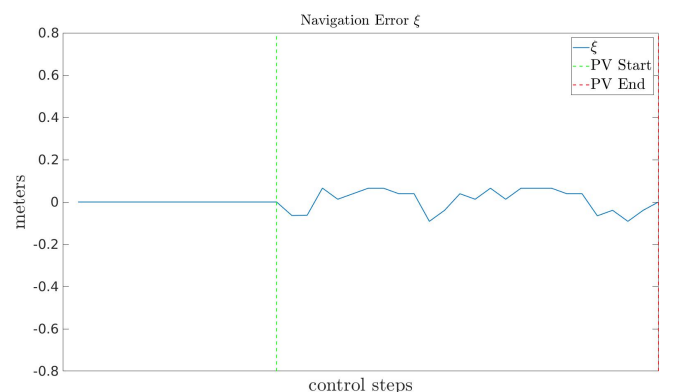
PV midline estimation and navigation. Once again, the UAV path is not reported since it would be difficult to appreciate differences with the previous tests.

In Figure 29, the control error e is shown, with $\mu_e = 0.038m$ and $\sigma_e = 0.054m$. In Figure 30, the navigation error ξ is shown, with $\mu_\xi = 0.05$ and $\sigma_\xi = 0.02$. The average navigation error is about half the previous cases, as visible in the Figure.

4) *Navigation with both cameras along 4 rows:* Additional experiments have been performed, using both cameras, along a longer path involving four rows, to confirm the capability

of the system to autonomously inspect PV plants. Figure 28 reports the UAV path corresponding to one of these experiments with a higher speed of $1.1m/s$.

Figure 29 reports the control error with average $\mu_e = 0.036m$ and standard deviation $\sigma_e = 0.051m$; Figure 30 reports the navigation error with average $\mu_\xi = 0.16m$ and standard deviation $\sigma_\xi = 0.14m$, which is higher than previous tests due to the increased speed. It can be observed that larger navigation errors can sometime occur, especially after moving from a row to the subsequent one using the embedded positioning system only (based on GPS, IMUs and compass);

Fig. 24. Control error from the estimated *PV midline* (RGB camera).Fig. 27. Navigation error from the real *PV midline* (both cameras).

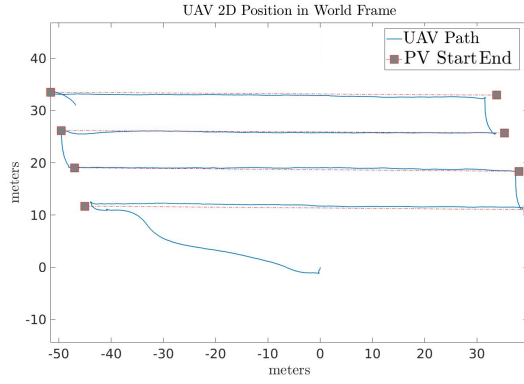
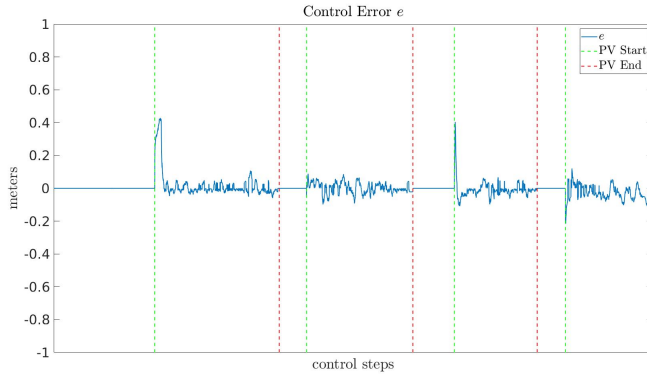


Fig. 28. Projection on the XY-plane of the UAV path (both cameras).

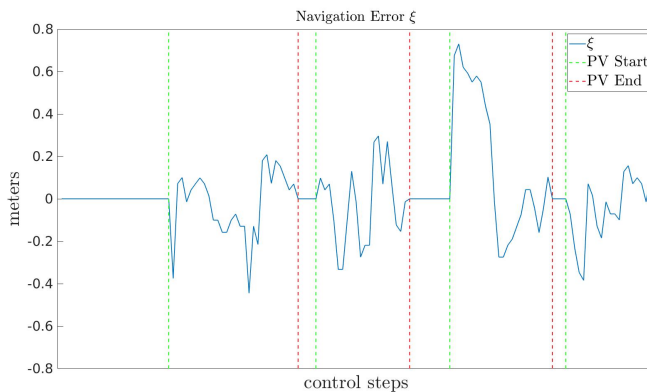
Fig. 29. Control error from the estimated *PV midline* (both cameras).

however, such error is bounded and the system is able to recover from it.

Finally, tests have been performed with a higher speed of 2.3m/s , resulting in a control error with average $\mu_e = 0.081\text{m}$ and standard deviation $\sigma_e = 0.129\text{m}$ and a navigation error with average $\mu_\xi = 0.28\text{m}$ and standard deviation $\sigma_\xi = 0.42\text{m}$.

VII. CONCLUSION

In this article, we presented a new approach for autonomous inspection of a PV plant using UAVs, based on the detection of PV modules through thermal and RGB cameras.

Fig. 30. Navigation error from the real *PV midline* (both cameras).

The proposed approach is based on:

- a segmentation algorithm based on thermal and RGB cameras;
- an EKF for the estimation of the *PV midline*, a straight line describing a PV module row;
- an algorithm for path following, whose input is a sequence of waypoints that describe a boustrophedon path to be followed in the PV plant, based on visual servoing when moving along a PV module row and on simple geometric considerations when moving from a row in the PV plant to the next one.

The system has been tested both in simulation and in a real PV plant with a DJI Matrice 300. Results suggest that the solution proposed meets the constraints for autonomous PV inspection, producing navigation errors that are sufficiently small to keep the PV modules within the camera field of view (which is mandatory for the acquisition and stitching of high-resolution thermal images for defect detection). Most importantly, navigation errors are small even in presence of errors in waypoint positions. Georeferenced waypoints computed from Google Earth images and GPS data may be affected by large biases but tend to be locally coherent: results confirm that alternating (i) visual servoing along a PV row with (ii) GPS-based navigation when moving from one row to the subsequent one, turns out to be a feasible solution.

During tests we observed that the use of both cameras, as expected, has a positive impact in reducing average errors. Additionally, we conjecture that using two sensors based on completely different principles for PV module segmentation can make the whole process more reliable when thermal or lighting conditions are suboptimal. For example when the PV panel heat may not be clearly distinguishable from the surrounding environment (e.g., early in the morning, especially in winter) or when sun glares can negatively affect color-based segmentation. Please notice that smaller navigation errors allows the UAV to flight at a lower height from the ground, a competitive advantages respect to solutions using GPS-based navigation along the whole path: a lower height from the ground enables collecting higher-resolution images of the plant, which is key to improve the detection of defects.

As future work, we are working to define planning procedures to process Google Earth images and automatically extract a sequence of georeferenced waypoints, a task that is far from being straightforward because the PV plant might have an irregular shapes, built on non flat terrain, and traversed by roads or power line infrastructures: PV rows are not necessarily arranged in the best way to be covered following a boustrophedon path. Also, even if we argue that a model-based approach offers many advantages in the considered scenario, still we are planning to evaluate Machine Learning techniques for PV module segmentation as a future work. This will enable a fairer comparisons on the field between model- and data-driven approaches in the context of autonomous, UAV-based inspection of PV plants.

REFERENCES

- [1] H. R. and F. D., *Our Renewable Future: Laying the Path for One Hundred Percent Clean Energy*. Island Press, 2016.

- [2] "Eurostat: Renewable energy statistics." [Online]. Available: https://ec.europa.eu/eurostat/statistics-explained/index.php?title=Renewable_energy_statistics
- [3] G. Petrone, G. Spagnuolo, R. Teodorescu, M. Veerachary, and M. Vitelli, "Reliability issues in photovoltaic power processing systems," *IEEE T. Ind. Electron.*, vol. 55, no. 7, pp. 2569–2580, 2008.
- [4] F. Grimaccia, S. Leva, A. Dolara, and M. Aghaei, "Survey on pv modules common faults after om flight extensive campaign over different plants in italy," *IEEE J. Photovolt.*, vol. 7, no. 3, pp. 810–816, 2017.
- [5] J. A. Tsanakas, L. Ha, and C. Buerhop, "Faults and infrared thermographic diagnosis in operating c-si photovoltaic modules: A review of research and future challenges," *Renew. Sust. Energ. Rev.*, vol. 62, pp. 695–709, 2016.
- [6] P. B. Quater, F. Grimaccia, S. Leva, M. Mussetta, and M. Aghaei, "Light unmanned aerial vehicles (uavs) for cooperative inspection of pv plants," *IEEE J. Photovolt.*, vol. 4, no. 4, pp. 1107–1113, 2014.
- [7] V. Carletti, A. Greco, A. Saggese, and M. Vento, "Multi-object tracking by flying cameras based on a forward-backward interaction," *IEEE Access*, vol. 6, pp. 43 905–43 919, 2018.
- [8] S. Djordjevic, D. Parlevliet, and P. Jennings, "Detectable faults on recently installed solar modules in western australia," *Renew. Energy*, vol. 67, pp. 215–221, 2014.
- [9] G. Roggi, A. Niccolai, F. Grimaccia, and M. Lovera, "A computer vision line-tracking algorithm for automatic uav photovoltaic plants monitoring applications," *Energies*, vol. 13, no. 4, 2020.
- [10] S. Hartmut, H. Dirk, S. Blumenthal, T. Linder, P. Molitor, and V. Tretyakov, "Teleoperated visual inspection and surveillance with unmanned ground and aerial vehicles," *Int. J. Online Biomed. Eng.*, vol. 13, pp. 26–38, 2020.
- [11] S. Rathinam, Z. Kim, A. Soghikian, and R. Sengupta, "Vision based following of locally linear structures using an unmanned aerial vehicle," in *CDC'05*, 2005, pp. 6085–6090.
- [12] E. Honkavaara, H. Saari, J. Kaivosoja, I. Pölönen, T. Hakala, P. Litkey, J. Mäkinen, and L. Pesonen, "Processing and assessment of spectrometric, stereoscopic imagery collected using a lightweight uav spectral camera for precision agriculture," *Remote Sens.*, vol. 5, no. 10, pp. 5006–5039, 2013.
- [13] N. Metni and T. Hamel, "A uav for bridge inspection: Visual servoing control law with orientation limits," *Autom. Constr.*, vol. 17, no. 1, pp. 3–10, 2007.
- [14] A. M. Moradi Sizkouhi, S. Majid Esmailifar, M. Aghaei, A. K. Vidal de Oliveira, and R. Rütger, "Autonomous path planning by unmanned aerial vehicle (uav) for precise monitoring of large-scale pv plants," in *PVSC'19*, 2019, pp. 1398–1402.
- [15] A. M. Moradi Sizkouhi, M. Aghaei, S. M. Esmailifar, M. R. Mohammadi, and F. Grimaccia, "Automatic boundary extraction of large-scale photovoltaic plants using a fully convolutional network on aerial imagery," *IEEE J. Photovolt.*, vol. 10, no. 4, pp. 1061–1067, 2020.
- [16] A. M. S. . M. A. S. M. Esmailifar, "Aerial imagery of pv plants for boundary detection," 2020.
- [17] S. A. Hassan, S. H. Han, and S. Y. Shin, "Real-time road cracks detection based on improved deep convolutional neural network," in *2020 IEEE Canadian Conference on Electrical and Computer Engineering (CCECE)*, 2020, pp. 1–4.
- [18] Y. Pan, X. Zhang, G. Cervone, and L. Yang, "Detection of asphalt pavement potholes and cracks based on the unmanned aerial vehicle multispectral imagery," *IEEE J. Sel. Top. Appl. Earth Obs. Remote Sens.*, vol. 11, no. 10, pp. 3701–3712, 2018.
- [19] F. Zhang, Y. Fan, T. Cai, W. Liu, Z. Hu, N. Wang, and M. Wu, "OTL-Classifer: Towards imaging processing for future unmanned overhead transmission line maintenance," *Electronics*, vol. 8, no. 11, 2019. [Online]. Available: <https://www.mdpi.com/2079-9292/8/11/1270>
- [20] S. Ren, K. He, R. Girshick, and J. Sun, "Faster r-cnn: Towards real-time object detection with region proposal networks," in *NIPS'15*, 2016.
- [21] A. Zormpas, K. Moirgiorgou, K. Kalaitzakis, G. A. Plokamakis, P. Partsiavelos, G. Giakos, and M. Zervakis, "Power transmission lines inspection using properly equipped unmanned aerial vehicle (uav)," in *IST'18*, 2018, pp. 1–5.
- [22] R. Duda and P. Hart, "Use of the hough transformation to detect lines and curves in pictures," *Commun. ACM*, vol. 15, no. 1, pp. 11–15, 1972.
- [23] J. A. Tsanakas, L. D. Ha, and F. Al Shakarchi, "Advanced inspection of photovoltaic installations by aerial triangulation and terrestrial georeferencing of thermal/visual imagery," *Renew. Energy*, vol. 102, pp. 224–233, 2017.
- [24] X. Li, Q. Yang, Z. Lou, and W. Yan, "Deep learning based module defect analysis for large-scale photovoltaic farms," *IEEE Trans. Energy Convers.*, vol. 34, no. 1, pp. 520–529, 2019.
- [25] A. Huerta Herraiz, A. Pliego Marug'an, and F. P. García Márquez, "Photovoltaic plant condition monitoring using thermal images analysis by convolutional neural network-based structure," *Renew. Energy*, vol. 153, pp. 334–348, 2020.
- [26] A. S. Vincenzo Carletti, Antonio Greco and M. Vento, "An intelligent flying system for automatic detection of faults in photovoltaic plants," *J. Ambient Intell. Humaniz. Comput.*, vol. 11, pp. 2027–2040, 2020.
- [27] A. Fernández, R. Usamentiaga, P. de Arquer, M. Fernández, D. Fernández, J. Carús, and M. Fernández, "Robust detection, classification and localization of defects in large photovoltaic plants based on unmanned aerial vehicles and infrared thermography," *Appl. Sci.*, vol. 10, no. 17, 2020.
- [28] H. Ismail, M. Alhussein, N. Aljasmí, and S. Almazrouei, "Enhance pv panel detection using drone equipped with rtk," in *IMECE'20*, vol. 7A-2020, 2020.
- [29] T. Solend, H. Jonas Fossum Moen, and A. Rodningsby, "Modelling the impact of uav navigation errors on infrared pv inspection data quality and efficiency," in *PVSC'21*, 2021, pp. 991–996.
- [30] S. Rathinam, Z. Kim, A. Soghikian, and R. Sengupta, "Vision based following of locally linear structures using an unmanned aerial vehicle," in *CDC'05*, 2005, pp. 6085–6090.
- [31] R. Raguram, J.-M. Frahm, and M. Pollefeys, "A comparative analysis of ransac techniques leading to adaptive real-time random sample consensus," in *ECCV'08*, D. Forsyth, P. Torr, and A. Zisserman, Eds. Berlin, Heidelberg: Springer Berlin Heidelberg, 2008, pp. 500–513.
- [32] A. Majeed, M. Abbas, F. Qayyum, K. T. Miura, M. Y. Misro, and T. Nazir, "Geometric modeling using new cubic trigonometric b-spline functions with shape parameter," *Mathematics*, vol. 8, no. 12, 2020.
- [33] J. A. Sarapura, F. Roberti, R. Carelli, and J. M. Sebastián, "Passivity based visual servoing of a uav for tracking crop lines," in *RPIC'17*, 2017, pp. 1–6.
- [34] G.-Y. Li, R.-T. Soong, J.-S. Liu, and Y.-T. Huang, "Uav system integration of real-time sensing and flight task control for autonomous building inspection task," pp. 1–6, 2019.
- [35] L.-C. Chen, Y. Zhu, G. Papandreou, F. Schroff, and H. Adam, "Encoder-decoder with atrous separable convolution for semantic image segmentation," in *ECCV'18*, 2018.
- [36] G. Roggi, A. Niccolai, F. Grimaccia, and M. Lovera, "A computer vision line-tracking algorithm for automatic UAV photovoltaic plants monitoring applications," *Energies*, vol. 13, no. 4, 2020.
- [37] Z. Xi, Z. Lou, Y. Sun, X. Li, Q. Yang, and W. Yan, "A vision-based inspection strategy for large-scale photovoltaic farms using an autonomous UAV," in *DCABES'18*, 2018, pp. 200–203.
- [38] A. Barredo Arrieta, N. Díaz-Rodríguez, J. Del Ser, A. Bénéttot, S. Tabik, A. Barbado, S. García, S. Gil-Lopez, D. Molina, R. Benjamins, R. Chatila, and F. Herrera, "Explainable explainable artificial intelligence (XAI): Concepts, taxonomies, opportunities and challenges toward responsible ai," *Inf. Fusion*, vol. 58, pp. 82–115, 2020.
- [39] S. Thys, W. Ranst, and T. Goedeme, "Fooling automated surveillance cameras: Adversarial patches to attack person detection," in *CVPR'19*, vol. 2019-June, 2019, pp. 49–55.
- [40] A. Haponik, "Fly to the sky! With AI. How is artificial intelligence used in aviation?" [Online]. Available: <https://addepto.com/fly-to-the-sky-with-ai-how-is-artificial-intelligence-used-in-aviation/>
- [41] S. Schirmer, C. Torens, F. Nikodem, and J. Dauer, "Considerations of artificial intelligence safety engineering for unmanned aircraft," in *SAFECOMP'18*, B. Gallina, A. Skavhaug, E. Schoitsch, and F. Bitsch, Eds. Cham: Springer International Publishing, 2018, pp. 465–472.
- [42] Stanford Artificial Intelligence Laboratory et al., "Robotic operating system." [Online]. Available: <https://www.ros.org>
- [43] C. Zhu, R. Byrd, P. Lu, and J. Nocedal, "Algorithm 778: L-BFGS-B: Fortran subroutines for large-scale bound-constrained optimization," *ACM Trans. Math. Softw.*, vol. 23, no. 4, pp. 550–560, 1997.
- [44] F. E. Daum, *Extended Kalman Filters*. London: Springer London, 2015, pp. 411–413. [Online]. Available: https://doi.org/10.1007/978-1-4471-5058-9_62
- [45] F. Capezio, A. Sgorbissa, and R. Zaccaria, "Gps-based localization for a surveillance ugv in outdoor areas," vol. 2005, 2005, pp. 157–162.
- [46] M. Aicardi, G. Casalino, A. Bicchi, and A. Balestrino, "Closed loop steering of unicycle-like vehicles via lyapunov techniques," *IEEE Robot. Autom. Mag.*, vol. 2, no. 1, pp. 27–35, 1995.
- [47] A. Sgorbissa, "Integrated robot planning, path following, and obstacle avoidance in two and three dimensions: Wheeled robots, underwater vehicles, and multicopters," *Int. J. Rob. Res.*, vol. 38, no. 7, pp. 853–876, 2019.